

A simulation model of biofilms with autonomous cells: I. Analysis of a two-dimensional version

Yergou B. Tatek, Gary W. Slater*

Department of Physics, University of Ottawa, 150 Louis-Pasteur, Ottawa, Ont., Canada K1N 6N5

Received 12 January 2005; received in revised form 8 July 2005

Available online 12 September 2005

Abstract

We introduce a single-cell based simulation model of biofilm growth. Each microbial cell is modelled as an autonomous agent whose behavior is controlled by thermodynamic parameters, mechanical properties, physiological rules and environmental conditions. In the two-dimensional version presented here, a cell is represented by a closed chain of self-avoiding beads linked together using the bond fluctuation algorithm. The cell is thus controlled both by the rigidity of its membrane and a pressure difference. The model is complemented by key features such as the explicit presence of nutrient diffusion and flow, the processes of cell-division and cell-death, and the attractive interactions between the cell and the surface on which the colony grows. Tuning the parameters of the model can lead to the growth and maturation of various types of biofilms. In this first article, we describe the main properties of a two-dimensional version of the model, and we discuss the extension to three dimensions.

© 2005 Elsevier B.V. All rights reserved.

Keywords: Biofilm; Bacteria; Monte Carlo simulation

1. Introduction

Biofilms are a common form of microbial community associated with surfaces in contact with liquids. For example, bacterial biofilms can be found growing in water pipes, on surgical instruments or on tooth surfaces. A distinguishing characteristic of biofilms is the presence of extracellular polymeric substances (EPS) in which the cells are embedded.

Mathematical models have been used for the last three decades in order to improve our understanding of the growth and behavior of microbial biofilms. Early models represented biofilms as spatially homogeneous steady-state films containing a single species [1]. Additional features, such as multiple types of nutrients, mixed microbial species and variable biofilm density were later included [2–4]. However, most of these models assumed a predetermined biofilm morphology. Consequently, they were unable to account for the experimentally observed 3D structural heterogeneity of the colonies. Furthermore, they made several assumptions about biofilm development. For instance, the direction of biomass displacement was taken to be

*Corresponding author. Tel.: +1 613 562 5800; fax: +1 613 562 5190.

E-mail addresses: yergou.tatek@science.uottawa.ca (Y.B. Tatek), gslater@science.uottawa.ca (G.W. Slater).

perpendicular to the substratum, while cell detachment was determined by an arbitrary uniform removal rate or velocity. Such simple models are generally suitable for representing the aggregate activity of a biofilm on many square millimeters of surface area.

In recent years, several biofilm numerical models which deal with smaller scales have been proposed. They can be divided into two classes of models, namely the continuum models and the discrete models. The continuum models use a mean-field-type of approach [5–7]. Most of the discrete models utilize methods, such as cellular automata, to simulate the rules that govern the lives of microbial cells. These coarse-grained models use a set of local rules governing the growth of the biomass, the displacement of the growing biomass as well as its detachment. These methods produce realistic, structurally heterogeneous biofilms [8–15] but a major drawback is that they rely on speculative rules which control the global biomass development [16] instead of the cell themselves. Another sub-class of discrete models are the so-called individual-based (or particle-based) models [17–19]. The latter approaches have some similarity with our model in that they consider cells as individual agents.

Our aim is to design and implement a new Monte Carlo model based on the life of autonomous cells in order to investigate the resulting bacterial populations (biofilms) static and dynamic characteristics. One of the features of our model is that nutrient mass transfer is implemented explicitly, i.e., we do not need to calculate the nutrient concentration field. Note that such a feature is also present in some other biofilm models [15]. However, we are aware of the fact that a complete integration of subcellular processes in our model (e.g., bacteria biochemistry) will be not only difficult but also rather useless; moreover, these complex biochemical subcellular processes are species-dependent. As our aim is to integrate cellular processes into a generic population model, we have taken a simple (not to say simplistic) view of a cell by treating it as a black box with simple thermodynamic properties and physiological rules. Thus, phenomena like metabolism and maintenance have been integrated in a simple fashion.

Current computational resources allow scientists to model complex ecological societies interacting with one another. Our approach follows similar lines. By creating models of cells that include, at the algorithmic level, the most important factors that control and mimic cell interactions, division, growth, and death, we will explore the formation and development of colonies (or biofilms) and examine how the various parameters that define the nature of the cells and their environment affect the final result. In this article, we will first introduce an approach which is capable of producing useful simulations of cells and biofilms. In order to obtain a computer model that can be used to simulate large populations of interacting cells (possibly of different species), the model must obviously be simple. We thus use a lattice Monte Carlo (LMC) model with elements borrowed from computational polymer science. The model can easily be programmed and generalized to complex situations while retaining simple rules that can be parallelized to use multiprocessor computers. Finally, we present results from a preliminary study of a two-dimensional (2D) version of the model. The emphasis of this first study will be on the thermo-mechanical aspects of single cells near walls, and on the general properties of small biofilm colonies growing on a flat surface.

2. The model

In order to design a reliable and computationally reasonable model of biofilms, we must do two things: (a) first, we must choose the proper computational approach, i.e., the appropriate level of coarse-graining for the physics involved; (b) then, we must identify the essential processes that we must keep in the model. The description presented in this section focuses on a 2D version of the model for simplicity. Some properties of 3D models will be discussed in the last section.

2.1. The bond-fluctuation algorithm

We employ a LMC algorithm to model the various physical elements of the biofilms. This approach is directly inspired from polymer science. The whole problem will be reduced to a list of rules that control how “particles” jump from site to site on a lattice. The particles can be linked together in various ways, may interact with each other through various potentials, and their net motion can be biased by external fields. Finally, the lattice itself must possess some boundary conditions. The model is thus fully defined by these

rules, links, potentials, fields and boundary conditions. LMC techniques are very efficient and allow a wide variety of natural phenomena to be studied.

Fig. 1 shows a simple 2D description of the bond-fluctuation algorithm (BFA) employed here [20]. The BFA uses a square lattice, and the smallest possible object is a single lattice plaquette (which we will call a monomer). Note that two monomers cannot share a lattice site: this defines volume exclusion between monomers. The motion of the monomers is limited to jumping by one lattice site along one of the four Cartesian directions ($\pm\hat{x}$ or $\pm\hat{y}$). Such a BFA jump is accepted only if it satisfies all conditions imposed by the local rules, such as volume exclusion and Metropolis energy tests [21].

A cell is defined by the membrane that separates its internal components from the external world. This membrane also modulates its interactions with other cells and surfaces, controls the exchange of material with its environment (including nutrients), and determines its mechanical properties. We thus need a representation of a membrane that will allow us to describe its properties using simple algorithmic rules. To achieve this, we will borrow computational tools from polymer science: the membrane will be a collection of BFA monomers

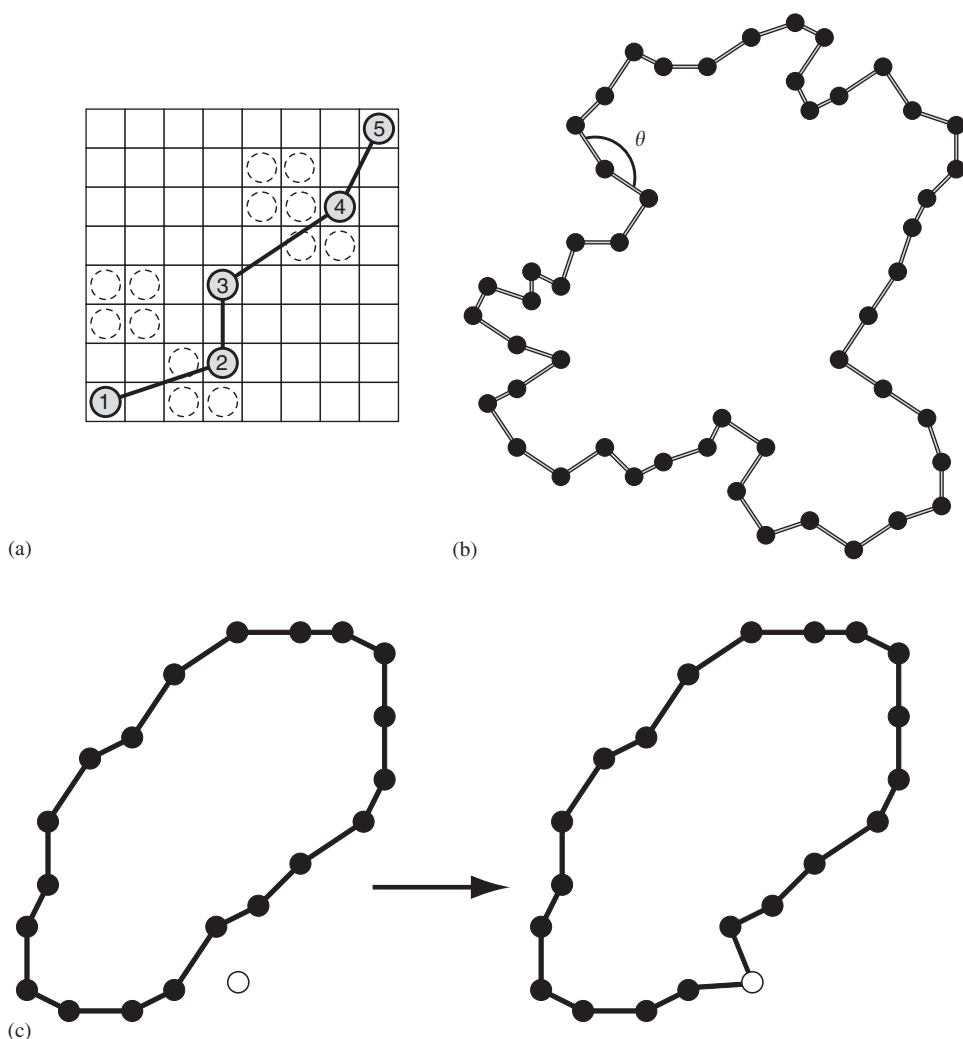


Fig. 1. (a) An illustration of the bond-fluctuation algorithm (BFA). The dashed circles represent the other sites where we could place monomers 2 and 4 without violating the BFA rules. (b) A ring BFA polymer, using our cell model; θ is the internal angle between two consecutive bonds. This example shows a random-walk cell with no bending potential and no internal pressure. (c) Cell growth: a new monomer is inserted between two consecutive monomers.

that we will link together by bonds to form a closed perimeter (Fig. 1b). As we will see later, cell division is easily implemented using this approach.

In the framework of the 2D BFA, the bond length ℓ between connected monomers is limited to lengths $2 \leq \ell \leq \sqrt{13}$. If monomers are not allowed to touch, this length restriction automatically insures that the BFA will respect chain connectivity and exclusion (i.e., chains will not cross each other). We also note that the BFA is known to be ergodic in both two and three dimensions [20]. In principle, one can associate an energy with the bonds such that bond stretching (or compression) costs energy. For example, we could use an harmonic potential of the form $U_\ell(\ell) = \frac{1}{2}k_\ell \times (\ell - \bar{\ell})^2$, where $\bar{\ell}$ is the average bond length. In fact, this is likely to be necessary for systems under large stresses because the BFA bonds cannot be stretched or compressed indefinitely. In some cases, one can even be faced with long-lived metastable states due to the systematic rejection of moves. In this introductory article, however, we will simplify the model by using simple situations where energy-free links do not lead to problems.

What makes our model different from existing biofilm models is that the mechanical aspects of the cell's membrane (e.g., membrane undulations) are explicitly taken into account. On the other hand, only a few free parameters are necessary. These parameters are summarized in Table 1. The following subsections describe how we model the various elements of the problem with a BFA algorithm that can be readily used to carry out extensive LMC simulations of biofilm growth and change. Note that all energies will be measured in units of $k_B T$ for simplicity.

2.2. The wall surface

Biofilms form on surfaces. The surface of the wall on which our simulation biofilms grow is simply a series of immobile and adjacent monomers (see Fig. 2a–c). The latter do not move during the simulations, but they can interact with all other objects in the simulations, as will be explained below (in particular, they can attract cell membranes). We will use the subscript w to refer to the wall properties. Note that the wall itself does not have to be physically and chemically flat. Indeed, the wall surface can be physically rough (with bumps and crevices) as well as chemically rough (interaction energies, attractive or repulsive, may vary from site to site). Rough surfaces are extremely interesting to study in the context of biofilm formation. In this article, though, we will look at simple flat surfaces for simplicity and we leave studies of rough walls for future investigations.

2.3. Cells

The cell membrane is thus essentially a ring polymer made of N_c monomers connected by N_c links. We use the subscript c to refer to the cell membrane. As we shall see, N_c is variable but must remain in the range

Table 1
An overview of some of the parameters of our model

Parameter	Comments
Maximum number of membrane monomers: N_c^0	N_c^0 is the size of a cell just after division (minimum cell size)
Cell osmotic pressure: p_c	$p_c \geq 0$
Maximum internal resources: N_{cs}^{max}	For the sake of simplicity, this value is independent of cell size
Interaction potentials: ε_{ij} with $i, j \in \{w, c, s\}$	There are five possible non-zero parameters
Minimum age to reach cell maturity: t_{mature}	The probability of cell division is non-zero passed this age once the cell is of size $2N_c^0$
Old age: t_{old}	The probability of cell death is non-zero passed this age
Tolerance to starvation: t_{famine}	The probability of cell death is non-zero passed this duration even if the cell has not yet reached the age t_{old}
Nutrient particles concentration: ρ	The concentration is kept constant by using particles reservoirs at constant concentration
Bias potential applied to the nutrient particles: U_s	We also use periodic boundary conditions

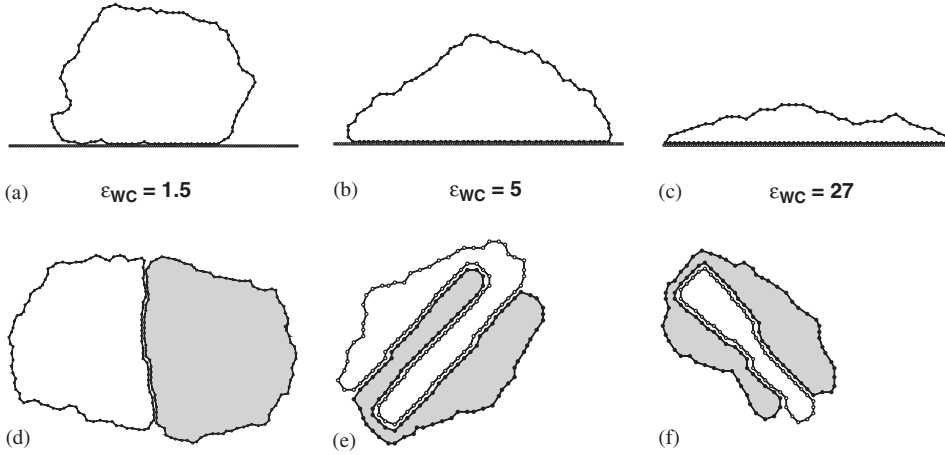


Fig. 2. Schematic picture showing various situations: (a) a cell is weakly adsorbed on a flat wall ($N_c = 100$); (b, c) the same cell is now strongly adsorbed and deformed; (d) two identical cells attract each other ($N_c^1 = N_c^2 = 100$); (e) the same two cells, but with a strong attraction; (f) two dissimilar cells and a strong attraction ($N_c^1 = 100 = 2N_c^2$).

between N_c^0 and $2N_c^0$, where N_c^0 is the minimum cell size. These BFA monomers are allowed to move according to the BFA rules described above. However, this would not be sufficient since ring polymers do not behave as living cells. For instance, ring polymers do not have internal pressure (as a result, they tend to collapse; see Fig. 1b) and they do not resist mechanical deformation (except for the entropic forces generated by deformations that reduce the entropy of the closed random-walk). We thus add two other features. First, we add a bending energy between two consecutive bonds:

$$U_c(\theta) = \kappa_c \times (1 + \cos \theta)^2, \quad (1)$$

where κ_c is the membrane bending rigidity parameter, θ is the angle between two consecutive bonds (see Fig. 1b). Such bending potentials generate semi-flexible polymer chains that can be characterized by a Kuhn length [22] $b_K(\kappa_c)$. When the membrane perimeter $N_c \bar{\ell}$ is much larger than the Kuhn length b_K , the equilibrium shape of the cell is essentially a circle (with thermodynamic fluctuations). However, the situation is different in the opposite case where the perimeter is not much larger than the Kuhn length: we then find that the equilibrium shape of the cell is often close to a regular polygon (e.g., a triangle or a square) with sides roughly equal to the Kuhn length itself (not shown). As these shapes are not realistic, we will avoid the conditions that lead to them.

Secondly, as our cells are closed entities it is assumed that there is an osmotic pressure difference across their membrane; this can be expressed by

$$p_c = p_{int} - p_{ext}. \quad (2)$$

Thus, the Hamiltonian associated with each cell can be expressed as

$$H = -p_c A + \sum_{i=1}^{N_c} U_c(\theta_i), \quad (3)$$

where A is the area of the cell. The present cell model shares some common features with previous vesicle models [23,24].

2.4. Mass transfer and uptake

Substrate particles (“food”), which are represented as single monomers, are allowed to diffuse freely on the lattice, subject to the BFA rules. In order to model a flow (if any), the motion of the substrate particles (subscript s) is biased by an external potential gradient U_s that can be used together with the Metropolis rule to choose the direction of the jumps. The boundary conditions are adjusted so that we have either a constant

number of particles entering the system per unit time (for cases with flows) or the concentration of particles is constant far from the colony (no flow conditions). Note that it is quite easy to generalize the model to include many varieties of substrate particles (including cell waste, signaling molecules for quorum sensing purposes, inhibitors, etc.) with various properties and interactions. If one wants to apply periodic boundary conditions for the substrate particles, it is necessary to ensure that the simulation box size is much larger than the colony size. Note that since the colony growth takes place on a wall surface, we actually simulate the system between two parallel walls to simplify the boundary conditions in this direction of space.

Cells must absorb substrate particles for three reasons: (i) to maintain their metabolism; (ii) to feed the growth of the cell membrane and volume; (iii) to eventually allow cell division. Substrate particles are thus allowed to cross cell membranes with a certain probability Γ_{cs} (also called substrate uptake probability) if they collide with the membrane. If a particle is allowed to cross the membrane, it is automatically taken out from the simulation box and a nutrient particles counter linked to the cell is incremented by one unit. This particles counter gives the number N_{cs} of nutrient particles which can be used by the cell, and therefore represents the “level of nutrition” (or stored energy) of the given cell. The uptake probability is itself proportional to the difference between the number of substrate particles already inside the cell (N_{cs}) and the maximum number N_{cs}^{max} allowed for the given cell size N_c (such that the cell stops absorbing new substrate particles past a certain point):

$$\Gamma_{cs} = \Gamma_{cs}^0 \times \left(1 - \frac{N_{cs}}{N_{cs}^{max}}\right). \quad (4)$$

Accordingly, Γ_{cs}^0 is the maximum uptake probability for the cell. A nutrient particle crossing the cell membrane is automatically considered to be part of the biomass.

2.5. Local interactions

All monomers (be they part of the substrate (s), the wall surface (w) or the cell membrane (c)) can interact with all the other monomers through interaction potentials. In this introductory study, we will consider only short-range interactions between monomers that are nearest-neighbors on the lattice (distance of $\Delta r = 2$ lattice sites). Therefore, the interaction potential between any two monomers will be written as

$$U_{ij}(\Delta r) = \varepsilon_{ij} \times \delta_{\Delta r, 2}, \quad (5)$$

where i and j are the indices indicating the nature of the two monomers involved and δ is the Kronecker Delta. In this model, $i, j \in \{w, c, s\}$. This defines a maximum of five different interaction parameters ε_{ij} (ε_{ww} being irrelevant). In practice, several of these parameters can either take the same value or be chosen equal to zero. As usual with LMC simulations, the BFA moves are then subject to Metropolis energy tests [21].

2.6. Cell growth, division and death

The state of a cell is defined by three critical numbers: its current age t , its perimeter (or size) N_c and its metabolic state as characterized by its internal content N_{cs} . Naturally, growth, division and death are related to these parameters.

Cell growth occurs simply by adding a monomer to the perimeter ($N_c \rightarrow N_c + 1$). This can easily be done within the framework of the BFA (see Fig. 1c). The new perimeter monomer is taken from the cell internal resources ($N_{cs} \rightarrow N_{cs} - 1$). The probability of cell growth per unit time, Γ_c increases linearly with N_{cs} , but decreases to zero when N_c is twice its initial value N_c^0 (see below):

$$\Gamma_c = \begin{cases} \Gamma_c^0 \times \frac{(2N_c^0 - N_c)}{N_c^0} \times \frac{N_{cs}}{N_{cs}^{max}} & \text{for } N_c < 2N_c^0, \\ 0 & \text{for } N_c = 2N_c^0. \end{cases} \quad (6)$$

A cell reaches maturity when the following two conditions are met: (i) its age exceeds a minimum value t_{mature} and, (ii) its perimeter reaches its maximum value $N_c^{max} = 2 \times N_c^0$. When both conditions are met, the

probability of cell division per unit time Γ_{div} becomes non-zero. Although cells do not stop growing while they are dividing, we have, in our model not allowed membrane growth during the division process. The dynamics of cell division is as follows. First, we pick two adjacent monomers at random and locate the two monomers that are N_c^0 monomers away on the membrane. The motion of these two pairs of monomers is then biased in such a way that they move towards one another (see Fig. 3). Once these monomers are within a distance $\leq \sqrt{13}$ of each other, we break the BFA bonds and rearrange them in such a way that two daughter cells with N_c^0 membrane monomers each are formed. This mimics fairly well the actual cell division process of a real cell. Of course, this process leads to two daughter cells (each with an initial age $t = 0$) with potentially different surface areas and internal contents N_{cs} (the internal resources N_{cs} of the mother cell are divided randomly among the two daughter cells). From this asymmetry and the fact that $\Gamma_c < 1$, growth synchrony is lost relatively quickly. Since the daughter cells will eventually want to grow again, a large amount of internal pressure will build up as the two cells feed on the local nutrients, and the system will relax by pushing the colony material away to create the space to fully accommodate the new and growing cells. Unlike some previous models, our system will equilibrate itself without the need for ad hoc rules governing colony adjustment. The volume expansion of the colony is therefore caused by the internal pressure generated by the growing biomass. This colony spreading mechanism is possibly the closest to the real mechanism [25].

Cell death occurs through two different channels: (i) after a certain critical age $t = t_{old}$, with $t_{mature} < t_{old}$, the cell has a finite probability Γ_{death} of dying per unit time; (ii) if N_{cs} is zero for a period of time exceeding a given threshold t_{famine} , the cell dies immediately (Table 2). Upon death, the cell is frozen in place for a finite period of time t_{frozen} , and then disintegrates into small pieces (we remove the links between the cell membrane monomers

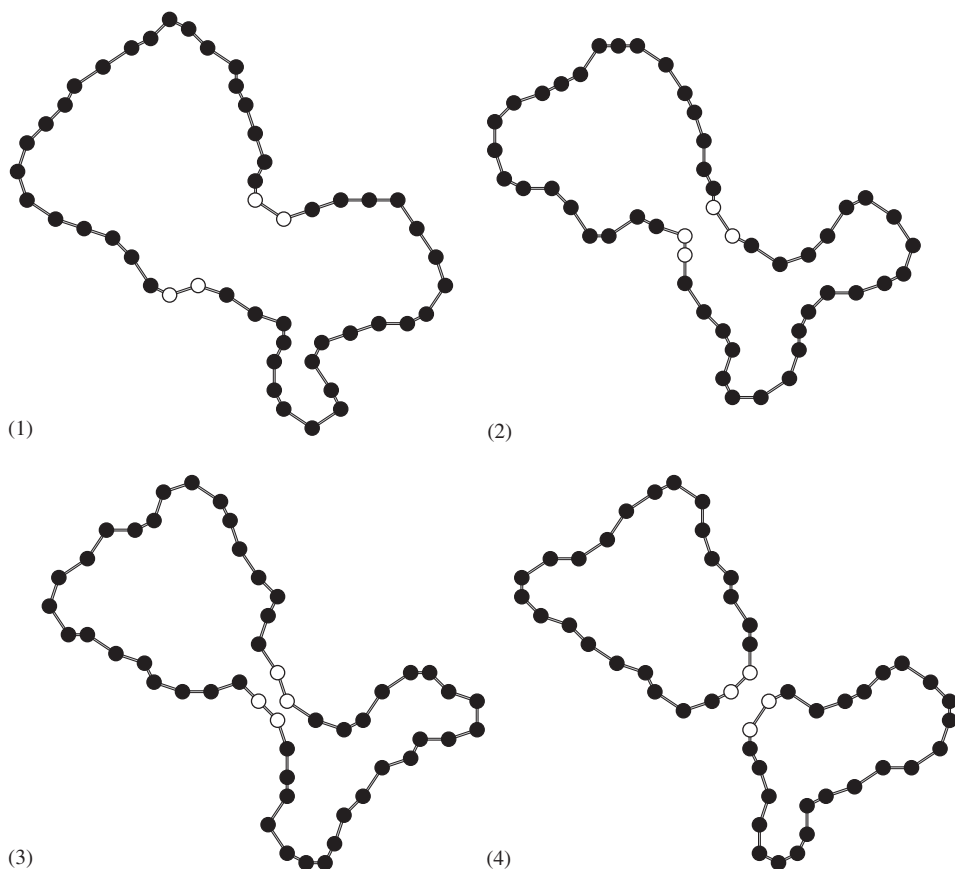


Fig. 3. Schematic diagram showing the various stages of a cell division: (1) two pairs of monomers are selected; (2) and (3) the biased motion of the two pairs of monomers towards each other; (4) new bonds are formed and two new daughter cells are born.

Table 2
An overview of the rate functions used

Function	Equation
Cell growth probability per unit time	$\Gamma_c = \Gamma_c^0 \times (2N_c^0 - N_c) \times N_{cs} / (N_c^0 \times N_{cs}^{max})$
Substrate uptake probability	$\Gamma_{cs} = \Gamma_{cs}^0 \times (1 - N_{cs} / N_{cs}^{max})$
Cell division probability per unit time	Γ_{div}
Cell death probability per unit time from starvation	$\Gamma_{starvation}$
Cell death probability per unit time for $t > t_{old}$	Γ_{death}

to form single and free monomers; in the simulations presented in this paper, these monomers then become nutrients for the surviving cells).

2.7. Detachment

Biofilm or cell detachment is viewed as a mechanistic process completely dependent upon the shear stress induced by the flowing bulk liquid, the competing interactions and the fluctuations of the membrane-wall interfacial interactions. In our computational model, the flow is represented by the biased displacement of the substrate particles under the influence of the external potential U_s . Hence, unlike other models, no ad hoc detachment rules have been adopted [26]. Instead, detachment would occur as a natural outcome of the competition between the cell–wall and cell–cell adhesion processes (due to the short-range interaction parameter ε_{cw} for example), on the one hand, and the flow-driven forces applied to the cell on the other hand. An improvement would be the addition of a chemically mediated detachment mechanism which could play an important role in some circumstances [27,28].

2.8. Time versus Monte Carlo steps

As usual for LMC methods, time is measured in so-called Monte Carlo steps (MCS). One MCS consists in one move attempt per monomer in the system (the monomer can be part of the membrane or the substrate). Consequently, there is only one time scale in the present model. Note that all monomers have the same jump frequency in the present version of the model; this simplification is not necessary and one may indeed give priority to some types of monomers (e.g., nutrients) over others (e.g., membranes) to better mimic the various time scales in the problem.

3. An analysis of the elements of the model

Extensive studies of the properties of 2D vesicles (which can be defined as ring-polymers subject to an internal pressure) have previously been reported by several other groups. Of particular interest here are the universal properties of flexible vesicles which have been explored both analytically and by Monte Carlo simulations. MC simulations have allowed to establish phenomenological scaling relations for vesicles with bending rigidity and osmotic pressure [23,24,29]. In this subsection we first test the validity of our cell model (a simple ring polymer chain) by comparing some basic results with literature data. We then look at different aspects of cell properties, looking for simulation parameters that may provide realistic cell models, and we finish by showing an example of colonies obtained by tuning some parameters of the systems. In all our simulations, we have used a minimum of 10^6 MCS for the initial equilibration phase, followed by at least $1-10 \times 10^6$ MCS for the data acquisition stage.

3.1. Internal pressure, membrane undulations and cell shape

In this subsection, we focus our attention on the surface area (A) of a single cell, but we also monitored the cell's radius of gyration (R_g). To calculate these geometric properties, we used the

following expressions:

$$A = \frac{1}{2} \left| \sum_{i=1}^{N_c-1} \mathbf{r}_i \times \mathbf{r}_{i+1} \right|, \quad (7)$$

$$R_g^2 = \frac{1}{N_c} \sum_{i=1}^{N_c} (\mathbf{r}_i - \mathbf{r}_{\text{CM}})^2, \quad (8)$$

where \mathbf{r}_i is the position of the i th monomer, and \mathbf{r}_{CM} is the position of the center of mass of the cell. We carried out extensive Monte Carlo simulations for cell sizes N_c ranging from 10 to 400 monomers.

We first test our algorithm by investigating the limit of weak (essentially negligible) bending rigidities ($\kappa_c = 0.005$) and zero osmotic pressures ($p_c = 0$). In such cases, our cell membrane is actually a 2D ring polymer, a well-studied system in polymer science. Fig. 4 presents distributions of surface areas A for membranes of different sizes under these conditions (top panel). The probability distribution functions (PDF) look like Gaussian distributions with a small positive skew, and they clearly broaden for increasing membrane sizes N_c . In other words, larger membranes undergo larger absolute shape fluctuations. For this simple low-stress situation, the mean square radius of gyration, the mean surface area and the corresponding standard-deviations follow the standard scaling laws

$$\langle R_g^2 \rangle \sim \langle A \rangle \sim \sqrt{\langle \Delta R_g^2 \rangle} \sim \sqrt{\langle \Delta A^2 \rangle} \sim N_c^{2\nu}, \quad (9)$$

where ν is the Flory exponent for (open) self-avoiding walks. We obtain $\nu = 0.75 \pm 0.01$ (the data for $\langle A \rangle$ are shown in Fig. 5, lower curve), in good agreement with theoretical and simulation results obtained for the scaling behavior of a D -dimensional surface embedded in d -dimensional space

$$\nu = \frac{2 + D}{2 + d}. \quad (10)$$

Here, with $D = 1$ and $d = 2$, this predicts a Flory exponent $\nu = \frac{3}{4}$, a result that is known to be exact [30,31]. If we define the relative cell shape fluctuations as the ratio $\sqrt{\langle \Delta A^2 \rangle} / \langle A \rangle$, we see from Eq. (9) that this quantity is independent of the size of the cell in this limit (this *lack of self-averaging* is a characteristic of random walks).

More important here is the behavior of our model cell in the presence of non-negligible bending rigidity and/or internal pressure. Indeed, the cell contour shape changes from rugged to smooth when either of these stresses (p_c or κ_c) increases. This is illustrated in Fig. 6. At low pressure but large bending rigidity, the cell looks like

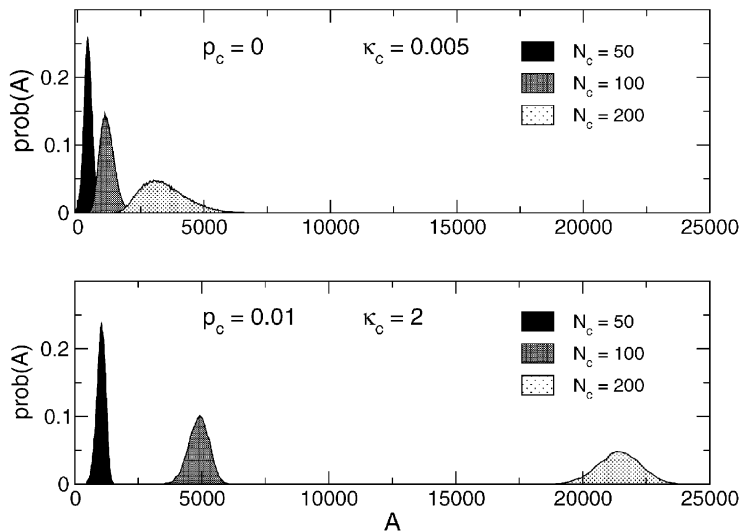


Fig. 4. Probability distribution functions (in arbitrary units) for the surface area A of cells with different sizes N_c (number of monomers) in the case of soft (top panel) and rigid (bottom panel) cells.

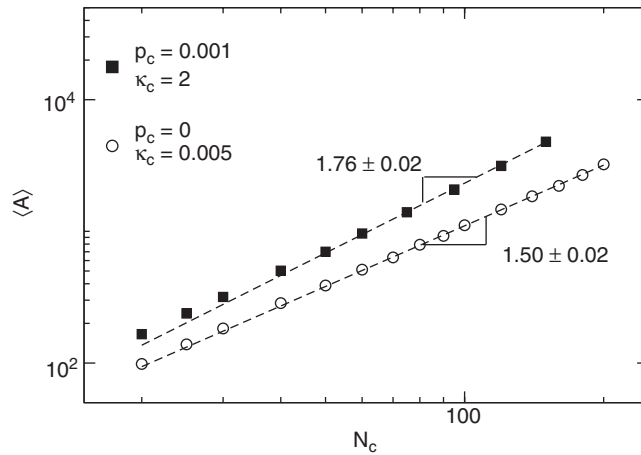


Fig. 5. Log-log plot of the mean surface area $\langle A \rangle$ against the size N_c for cells with two different values of κ_c and p_c . Linear fits of the large N_c data are also shown. Note that the cells are in the soft regime.

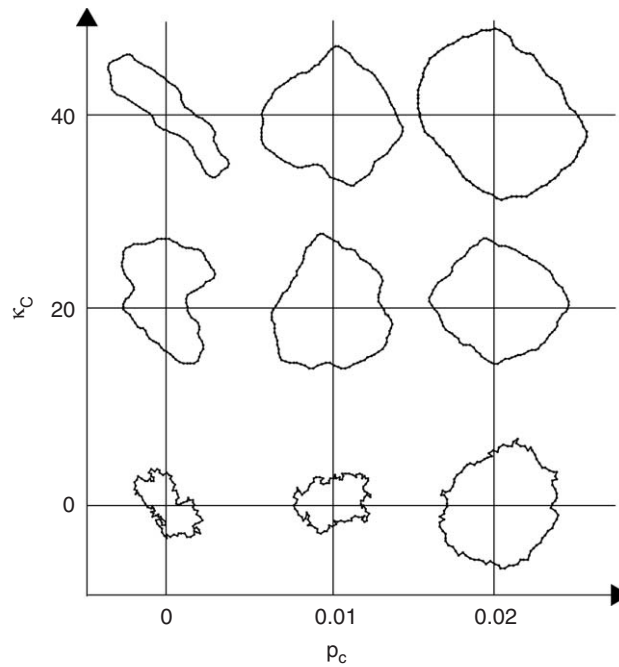


Fig. 6. Typical cell shapes for various regions in the κ_c - p_c phase space. All cells have $N_c = 100$ monomers.

a smooth deflated balloon. In the opposite situation (high pressure but low bending rigidity), the cell tends towards a circular shape with some sharp kinks. Finally, when both p_c and κ_c are large, the cell takes a non-physical square shape oriented at 45° (an artefact of the bond fluctuation algorithm and the square lattice).

The effects of the pressure and the bending rigidity on the cell shape have two important consequences. First, Eq. (9) is no longer valid. Instead, fitting simulation data with the empirical scaling law $\langle A \rangle \sim \langle R_g^2 \rangle \sim N_c^{2\nu}$ provides, at least over a restricted range of cell sizes N_c , an effective exponent ν that slowly increases towards $\nu = 1$ (typical of a smooth inflated 2D shape) as the internal cell stress increases (see, for example, the upper curve in Fig. 5). Note that ν actually increases slowly for larger N_c (this can also be seen in Fig. 5); the reasons for this will be discussed later in this subsection. Second, the cell's average surface area $\langle A \rangle$ increases while its relative shape fluctuations $\sqrt{\langle \Delta A^2 \rangle} / \langle A \rangle$ are greatly reduced (see Fig. 4, bottom panel).

A simpler way to look at these two effects simultaneously is provided by Fig. 7, a plot of the average surface area and its standard-deviation as a function of κ_c . We note that the standard-deviation (filled symbols and right vertical axis) reaches a maximum at a critical value $\kappa_c^*(p_c)$. This critical value is found to be smaller for larger internal pressures p_c . Membrane undulations increase in importance up to the critical bending rigidity κ_c^* , and then decrease steadily afterwards. Therefore, κ_c^* marks a transition towards a *rigid phase*. This transition happens earlier at higher internal pressure because the pressure stretches the membrane and adds to its rigidity. A similar situation exists if one fixes the bending parameter κ_c and varies the pressure p_c (results not shown); in particular, this defines a critical pressure $p_c^*(\kappa_c)$ beyond which the membrane is rigid. Note that these critical values vary significantly with cell size N_c . Indeed, while entropy loss upon cell swelling is proportional to N_c , the loss in surface potential energy varies like $Ap_c \sim N_c^{2\nu}$; this means that larger cells will require less pressure to reach the rigid phase. This also explains why the empirical exponent ν introduced previously increases slowly with size N_c .

Since the critical pairs (p_c^*, κ_c^*) are the same whether we scan κ_c and fix p_c , or vice versa (results not shown), we can use these critical values to draw a phase diagram, as shown in Fig. 8a for cell sizes $N_c = 20, 50$ and 100 . Below the critical lines, the cells are soft and flexible, and they resemble the closed self-avoiding polymer

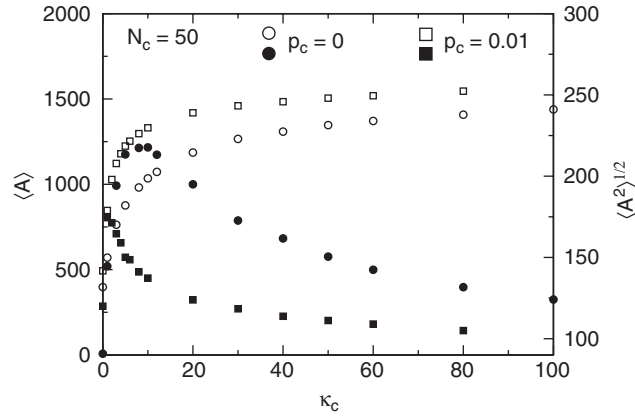


Fig. 7. The average surface area $\langle A \rangle$ (empty symbols) and its standard-deviation $\sqrt{\langle \Delta A^2 \rangle}$ (filled symbols) as a function of the bending potential κ_c for $N_c = 50$ and two different values of the internal pressure p_c .

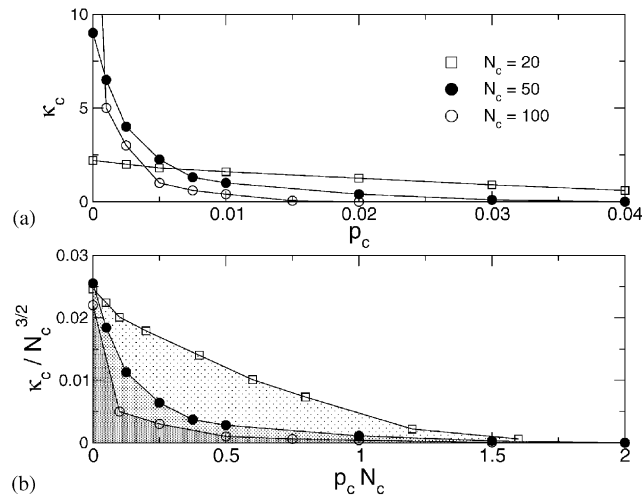


Fig. 8. The κ_c versus p_c phase diagram for cells of size $N_c = 20, 50$ and 100 . The lines separate the two different cell states: the soft state below the line and the rigid state above (see also Fig. 6). The raw data is presented in (a). In (b), the axes have been rescaled, as indicated, in order to make the three curves touch the two axes at approximately the same points.

chains shown in Fig. 6. Above the critical line, however, the cells are rigid, rather circular, and they undergo limited membrane undulations. In order to model cells, we generally use conditions that lead to mechanically rigid membranes, i.e., we use conditions that are above the critical line for the chosen minimum cell size N_c^0 (however, we avoid conditions that generate non-physical square cells). Note that we must make sure that this is also the case for the maximum cell size $2 \times N_c^0$ since N_c actually varies during the lifetime of the cell (one must be careful since the critical lines cross each other in the phase diagram in Fig. 8a).

It is interesting to note that the critical lines of the phase diagram are strong functions of the size N_c . The point p_c^0 where the critical line touches the p_c axis moves towards lower pressures for larger cell sizes because of the dominance of the pressure term Ap_c for large values of N_c ; empirically, we find an approximate scaling $p_c^0 \sim 1/N_c$. However, this is not symmetrical since the point κ_c^0 where the critical line touches the κ_c axis moves up for larger sizes N_c ; here, we find an approximate scaling law $\kappa_c^0 \sim N_c^{3/2}$. This is due to the fact that at zero pressure, the bending rigidity is the only factor that fights against the loss of entropy of the cell membrane when the latter becomes rigid; since entropy increases with N_c , we need larger values of κ_c to rigidify larger cells. Using these findings, it is possible to plot a rescaled phase diagram, Fig. 8b, which illustrates that the transition line is indeed not universal.

3.2. Adhesion of the membrane to a wall surface

In real systems, a cell membrane and a wall would interact via several different intermolecular forces such as van der Waals, electrostatic and structural forces. The effective interaction potential must exhibit a minimum near the wall so that the membrane adheres to the wall [32]. Since we are interested in the general characteristics of cell adhesion (in terms of binding and unbinding transitions, contact surface area, etc.), we use an effective contact potential energy ε_{wc} . Cell adhesion will generally depend upon the size of the membrane, the bending rigidity, the internal cell pressure and the adhesion energy.

First we look at cell adhesion (or adsorption) for a given cell size and bending rigidity ($N_c = 100, \kappa_c = 5$) and two internal pressures ($p_c = 0$, corresponding to a random walk cell, and $p_c = 0.01$, corresponding to a rigid membrane). Our aim is to investigate the effect of the monomer–wall interaction energy ε_{wc} on the adsorption of these two types of cells. We define the fraction of adsorbed monomers as $\gamma_{wc} \equiv N_c^{ads}/N_c$, where N_c^{ads} is the number of monomers in contact with the wall. As expected, $\langle \gamma_{wc} \rangle$ is an increasing function of the adhesion energy (Fig. 9). For the two cases shown here, the sigmoidal curves possess an inflection point around $\varepsilon_{wc} \cong 1.5$ (see below), curve very rapidly around $\varepsilon_{wc} \cong 5$, and are essentially flat for $\varepsilon_{wc} \gtrsim 15$. The inflection points indicate a unbinding–binding thermodynamic transition. Looking at the fluctuation parameter χ_{wc} defined by the relation

$$\chi_{wc}^2 \equiv \langle \gamma_{wc}^2 \rangle - \langle \gamma_{wc} \rangle^2 \quad (11)$$

not only confirms the existence of such a transition (see also the inset in Fig. 9) but also gives a more accurate value of the critical adsorption energy ε_{wc}^* . Indeed, the peaks in the χ_{wc} curves and the inflection points of the $\langle \gamma_{wc} \rangle$ curves are located at the same value of ε_{wc} . For example, we find here that the critical adsorption energies are $\varepsilon_{wc}^* \simeq 1.5 \pm 0.1$ in the ($\kappa_c = 5, p_c = 0$) case, and $\varepsilon_{wc}^* \simeq 1.4 \pm 0.1$ for the ($\kappa_c = p_c = 0.01$) case. We also note that the fluctuations amount to less than 1 monomer (i.e., $\chi_{wc} < 1/N_c$) when $\varepsilon_{wc} \gtrsim 8$, marking the beginning of a strong adsorption regime.

Also important is the total membrane energy

$$U_{tot} = \sum_{i=1}^{N_c} U_c(\theta_i) - (N_c^{ads} \times \varepsilon_{wc}) - (p_c \times A). \quad (12)$$

Its mean value per monomer is shown in Fig. 10 as a function of the interaction energy ε_{wc} . We can apparently distinguish two regimes corresponding to the unbound and bound states. The situation is more revealing when we look at the fluctuations χ_U of the total energy:

$$\chi_U^2 \equiv \langle U_{tot}^2 \rangle - \langle U_{tot} \rangle^2. \quad (13)$$

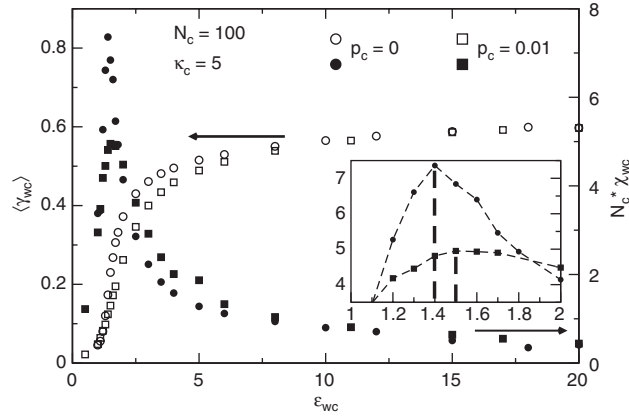


Fig. 9. Fraction of the average number of adsorbed monomers $\langle \gamma_{wc} \rangle$ (empty symbols) and the corresponding standard-deviation χ_{wc} (filled symbols) versus the wall–monomer interaction energy ϵ_{wc} for cells of size $N_c = 100$ and two different values of the pressure p_c . The inset shows a magnified view of the region near the maxima of the standard-deviation.

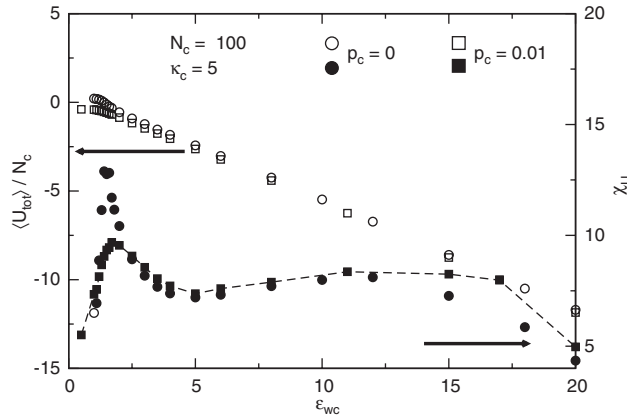


Fig. 10. Average of the total energy per monomer (open symbols) and its standard-deviation χ_U (filled symbols) as a function of the wall–monomer interaction energy ϵ_{wc} for $N_c = 100$ and two different values of the pressure p_c .

Fig. 10 also shows the dependence of χ_U upon the adhesion energy ϵ_{wc} . The curves have similar profiles for both pressures and we can now observe three different regimes. The first one corresponds to the unbound state where the bending and pressure terms account for almost all of the energy of the cell. In this first regime ($0 < \epsilon_{wc} < \epsilon_{wc}^* \cong 1.5$), the mean energy is small (note that it is actually positive at zero-pressure) and essentially independent of ϵ_{wc} , and the fluctuations increase rapidly. This is the regime where cells stick to the wall for finite periods of time. In the second regime, found in the region $\epsilon_{wc}^* < \epsilon_{wc} \lesssim 5$, the mean energy decreases almost linearly with ϵ_{wc} while the fluctuations drop quickly and go through a shallow minimum just before the point where $\chi_U = \epsilon_{wc} \cong 8$. We note that this is also the region where the value the $\langle \gamma_{wc} \rangle$ line curves rapidly in Fig. 9. We then observe a broad and rather flat secondary maximum (in the region $\epsilon_{wc} \cong 10$ –15); the fluctuations slowly decrease beyond this point, and the total energy decreases linearly with ϵ_{wc} since adhesion completely dominates the energetics. In this third regime, starting at about $\epsilon_{wc} = 8$, the energy fluctuations are weak (i.e., $\chi_U < \epsilon_{wc}$) and the corresponding monomer fluctuation are quite small (i.e., $\langle \gamma_{wc} \rangle < 1/N_c$); this is a “glassy” regime since the cell “foot” is essentially frozen.

In the second regime, the cell is in a dynamic bound state. This means that the main component of the observed energy fluctuations is the continuous adsorption/desorption of monomers. As the probability to have monomer desorption is proportional to $e^{-\epsilon_{wc}}$, monomers desorb less and less with increasing ϵ_{wc} . The last regime corresponds to an irreversible/quenched bound state and the very weak fluctuations we observe are

essentially due to the bending and pressure energy fluctuations of the non-adsorbed section of the cell. Note that the situation for $\varepsilon_{wc} \gtrsim 15$ is highly metastable and the simulation results generally depend upon the simulation time since no true equilibrium can be reached in most cases. In fact, the bound state is then irreversible and as soon as a monomer touches the wall, it stays bound to it. The cell thus deforms slowly to cover as much of the wall as possible (the edges slowly crawl outwards). Internal cell pressure and bending energies then form a potential barrier to slow down further monomer adsorption. Fig. 11 shows the variation of the total energy of a single cell as a function of the number of MCS (τ) for two wall–monomer interaction energies ($\varepsilon_{wc} = 5$ and 27). The profile of the curve in the strong interaction case illustrates the irreversibility of the adhesion process (the jumps are of size $\varepsilon_{wc} = 27$ and always downwards). Typical cell shapes are shown in Figs. 2(a–c) for three values of ε_{wc} . Fig. 12 shows the time evolution of the mean surface area of the cell–wall contact region (as measured by $\langle N_c^{ads}(\tau) \rangle / N_c$). All four curves have a typical sigmoidal shape, and the long-time plateau is higher for larger values of the binding energy (note that the mean values include only those cells that stayed in contact with the wall during the entire time period used here). The data appear to follow a power law $\langle N_c^{ads}(\tau) \rangle / N_c \sim \tau^b$ for intermediate times centered around the inflection point, with the exponent b increasing slowly from 0.28 ± 0.02 at the critical value $\varepsilon_{wc} = 1.5$ to 0.48 ± 0.02 at $\varepsilon_{wc} = 27$. These values are

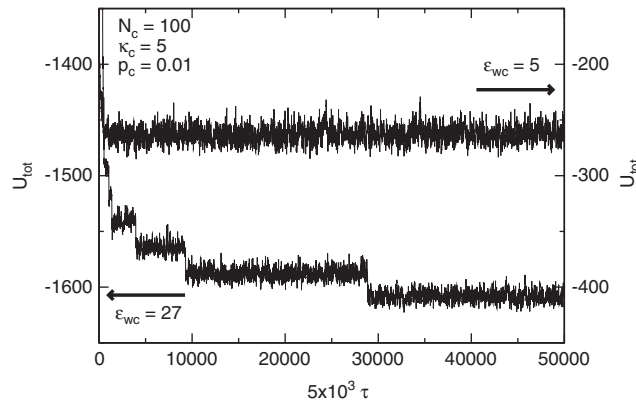


Fig. 11. Total energy U_{tot} of a rigid cell as a function of time τ (number of Monte Carlo Steps) for two values of ε_{wc} . The $\varepsilon_{wc} = 5$ cell has reached equilibrium. The $\varepsilon_{wc} = 27$ cell, however, is in a metastable state: U_{tot} still decreases by quanta of energy $\varepsilon_{wc} = 27$, and the fluctuations are due to the bending and pressure terms (they indeed are comparable to the fluctuations observed in the other case).

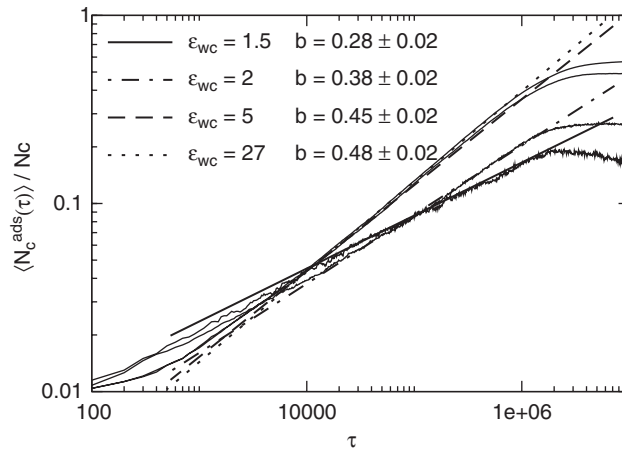


Fig. 12. Average fraction of adsorbed monomers for a cell as a function of time (number of Monte Carlo Steps) for four different values of ε_{wc} . The middle part of the sigmoidal curves can be fitted with a power law $\langle N_c^{ads}(\tau) \rangle \sim \tau^b$, as shown. The exponent b increases towards the value of $\frac{1}{2}$ for strong adsorption energies.

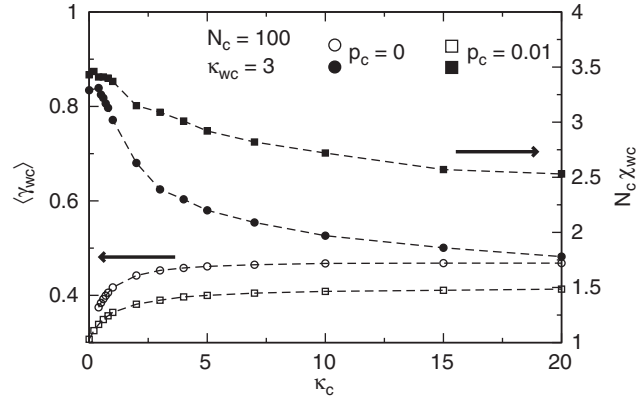


Fig. 13. Fraction of the average number of adsorbed monomers $\langle \gamma_{wc} \rangle$ (open symbols) and its standard-deviation χ_{wc} (filled symbols) as a function of the bending rigidity κ_c for two different values of the osmotic pressure p_c .

similar to those found recently by Döbereiner et al. [33] for what they call the basal phase of cell spreading. The fact that we do not find their intermediate phase of fast spreading is actually expected since the current version of our model does not describe cells with active spreading mechanisms such as actin polymerization.

As we said earlier, bending rigidity affects the adhesion process. For given values of the cell size N_c , the cell pressure p_c and the contact potential ε_{wc} , the fraction of adsorbed monomers *increases* and reaches a plateau with increasing κ_c . An example is shown in Fig. 13 for $N_c = 100$, $p_c = 0$ and $\varepsilon_{wc} = 3$. This somewhat counter-intuitive result is due to the reduced membrane undulations resulting from a more rigid bending potential (the fluctuation parameter χ_{wc} is also shown). Fewer undulations means a reduced entropic repulsion between the flat surface and the cell membrane. The opposite effect is observed when the internal pressure is changed (the case $p_c = 0.01$ is also shown): we observe a weaker tendency to adsorb to the wall when the pressure is increased since the cell tries to keep a more spherical shape at higher pressure. Therefore, cell adhesion must compete against natural cell undulations and the cell attempts to keep a circular shape. This can lead to fascinating effects as the physical conditions of the system evolve or when cells of different types compete for a limited surface area. Finally, it is interesting to note that the critical value $\varepsilon_{wc}^* \cong 1.5$ is a very weak function of the simulation parameters κ_c , p_c and N_c ; in fact, this critical value is what we also find for simple bond-fluctuation linear chains adsorbing on a flat surface (results not shown).

3.3. Cell–cell interactions

Two naked cells (i.e., cells without EPS polymers) interact directly via the contact potential ε_{cc} . This attractive force must compete against the entropic repulsion due to the membrane thermal undulations (the latter vary like the inverse of the membrane bending potential κ_c [34,35]). When ε_{cc} is small, the entropic forces limit the number of contacts between two interacting cells. Fig. 14 shows how the number of bound monomers N_{cc} varies with ε_{cc} when two cells, of sizes N_c^1 and N_c^2 , are in contact. We chose a case of two identical cells (of sizes $N_c^1 = N_c^2 = 100$) as well as a case of dissimilar cells where $N_c^2 = \frac{1}{2}N_c^1 = 50$, a situation that may happen when a mature cell is in contact with a newborn one. In order to compare the two cases more easily, we plotted the fraction of bound monomers, $\gamma_{cc} \equiv N_{cc}/(N_c^1 + N_c^2)$. In both cases, we can define three different regions for the $\langle \gamma_{cc} \rangle$ curves, separated by two maxima in the corresponding curves showing the evolution of the standard deviation χ_{cc} . These two peaks in the χ_{cc} curves are actually related to different transition types. The first one, which occurs at the critical energies $\varepsilon_{cc}^* \cong 1.6$ ($N_c^1 = N_c^2$) and $\varepsilon_{cc}^* \cong 1.75$ ($N_c^1 = \frac{1}{2}N_c^2$), corresponds to the unbinding–binding transition, whereas the second peak located at $\varepsilon_{cc}^{**} \cong 3.4$ ($N_c^1 = N_c^2$) and $\varepsilon_{cc}^{**} \cong 3.1$ ($N_c^1 = \frac{1}{2}N_c^2$) corresponds to a glassy transition. The region $\varepsilon_{cc} < \varepsilon_{cc}^*$ is characterized by reversible binding (the cells adhere to each other and move together for limited periods of time before getting free again). In the intermediate region $\varepsilon_{cc}^* \lesssim \varepsilon_{cc} \lesssim \varepsilon_{cc}^{**}$, where we observe a smooth increase of $\langle \gamma_{cc} \rangle$ somewhat similar to what we

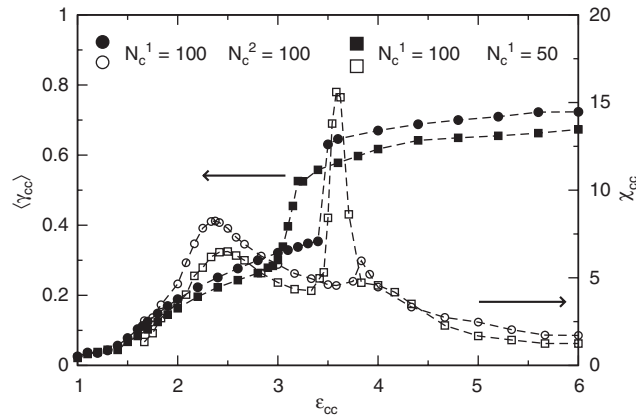


Fig. 14. Fraction of the average number of bound monomers $\langle \gamma_{cc} \rangle$ (filled symbols) and its fluctuations (open symbols) for two interacting cells of same and different sizes as a function of the attractive energy. In the two examples shown here, the values of the cells parameters are: $\kappa_c = 5$ and $p_c = 0.01$. The interacting cells undergo two successive transitions: an unbinding–binding transition and a glassy transition.

found for cell–wall interactions (Fig. 9), the cells remain in contact but their joint interface goes through large fluctuations, both in size and shape (Fig. 2d). The last region $\epsilon \gtrsim \epsilon_{cc}^{**}$, where $\langle \gamma_{cc} \rangle$ undergoes a remarkably sharp increase before reaching a plateau, is characterized by a glassy interface that traps defects for very long periods of time; the interface is essentially frozen. Moreover, the cells maximize the length of their interface by deforming and wrapping around each other (Fig. 2e–f). In practice, the last region is not appropriate for biofilms and we avoid choosing such conditions.

4. Some simple biofilms

Given the detailed study presented in Section 3, it is clear that the selection of the model parameters will be extremely important if we want to simulate the growth and development of physically meaningful biofilms. We can regroup the different parameters into the following five sets: the structural parameters, the interactions parameters, the age parameters, the rate parameters, and finally the external parameters. Some of these have a major impact on the final shape and size of a bacterial colony. For example, a low internal pressure tends to inhibit the cell division process, which leads to slow biofilm growth and extensive reorganization within the colony. The key parameters appear to be the cell structural parameters (κ_c and p_c), the interaction parameters (ϵ_{wc} and ϵ_{cc}), the characteristic ages (t_{mature} and t_{old}), and the nutrient concentration (which we will denote ρ). On the other hand, parameters such as the maximum cells size (N_c) do not play a crucial role.

In this section, we present preliminary results showing some biofilms obtained with several sets of parameters. We chose not to include the EPS in these simulations for simplicity. An extensive study of the colonies generated by our model will be presented in future articles. The default values (if not specified otherwise) of the parameters used for the simulations are given in Table 3. Below, we start by presenting a brief rationale for these choices.

The cell structural parameters: While low values of N_c^0 lead to rough polygonal cells, large values can increase the computing time substantially; $N_c^0 = 20$ was found to be a good compromise. The value of $N_{cs}^{max} = 20$ was selected for the same reasons. The pressure and bending parameters must be chosen to produce rigid cells. The phase diagram in Fig. 8 is needed here. We choose a fairly high pressure $p_c = 0.1$ and a bending energy $\kappa_c = 3$, which corresponds to a point well above the transition line for both $N_c = N_c^0 = 20$ and $N_{cs}^{max} = 2N_c^0 = 40$.

Interaction parameters: The interaction parameters actually play the most important role in this problem since they dictate how the cells and the wall will interact to form the final biofilm. As we saw, the cell–wall interaction energy ϵ_{wc} must be in the range $\simeq [1.5, 15]$ in order to allow for the growth of a biofilm on the surface. On the other hand, we are restricted to the range $1.6 \lesssim \epsilon_{cc} \lesssim 3$ if we are to generate dynamic colonies.

Table 3
Default values of the parameters used in the simulations presented in Section 4

Parameters	Values	Parameters	Values
N_c^0	20	Γ_{div}	0.5
κ_c	3	Γ_{death}	0.5
p_c	0.1	$\Gamma_{starvation}$	0.5
N_{cs}^{max}	20	Γ_c^0	10
ε_{wc}	2	Γ_{cs}^0	1
ε_{cc}	1.8	ρ	0.002
t_{mature}	$10 \times \tau_{food}$	U_s	0
t_{old}	$10^4 \times \tau_{food}$		
t_{famine}	$50 \times \tau_{food}$		
t_{frozen}	$0 \times \tau_{food}$		

The simulated colonies that we present differ in the choice of the pair $(\varepsilon_{wc}, \varepsilon_{cc})$ that we made. As we shall see, different combinations can lead to very different types of colonies.

Age parameters: In order to generate biofilms that have a good chance of growing to large sizes, we choose $t_{mature} < t_{famine} \ll t_{old}$. Finding actual numerical values for these parameters is a challenge. To do this, we need a fundamental measure of the rate at which events occur in the life of our model cells. A useful time scale can be defined as the time τ_{food} taken by a nutrient particle to diffuse randomly over a length scale comparable to the size of the cell. This essentially defines the natural diffusion-limited feeding rate in the system. For our cells, this is given roughly by

$$\tau_{food} \simeq \frac{\langle A \rangle}{D}, \quad (14)$$

where the mean surface area scales like N_c^{2v} and D is the diffusion coefficient of a free nutrient particle. With $\langle A \rangle \simeq 200$ and $D \simeq \frac{1}{4}$, we obtain $\tau_{food} \simeq 10^3$. We thus chose all of our cell age parameters to be much larger than 1000. Note that in all our simulations, we take $t_{frozen} = 0$, which means that when a cell attains t_{old} , it is immediately transformed into nutrient particles.

Rates: In order to speed up the simulations, we used very large values for the rate parameters. They include the cell division probability Γ_{div} , the cell death probabilities Γ_{death} and $\Gamma_{starvation}$, as well as the cell growth probability and the nutrient uptake probability prefactors Γ_c^0 and Γ_{cs}^0 , respectively.

External parameters: In this preliminary study, we will not include an external flow ($U_s = 0$). The simulation box uses two parallel walls facing each other, and periodic boundary conditions in the other direction. The colony will be made to grow on one of the walls. A reservoir of nutrient particles is placed at each end of the simulation box (see Fig. 15); note that the two reservoirs actually form a single unit because of the periodic boundary conditions. The reservoirs are kept at constant particle surface concentration ρ . New nutrient particles are thus injected periodically (every $0.1 \times \tau_{food}$ here) and randomly in the reservoir, as needed, so as to keep the reservoir concentration constant. We will compare the colonies obtained using a nutrient rich medium and a nutrient poor medium.

4.1. Colony patterns

The present model generates a wide range of colony morphologies as we will briefly see in this section. We have so far observed that at least three distinct colony patterns can be obtained by varying only two parameters: the cell–cell interaction energy (ε_{cc}) and the nutrient concentration (ρ). On the other hand, the cell–wall interaction energy does not seem to have a large influence on the biofilm structure.

Fig. 16a presents an example of biofilm in which cells interact weakly ($\varepsilon_{cc} = 1.6$). The cells are not densely packed even though there is little branching. However, the non-uniformity of the biofilm contour is reminiscent of Eden clusters [36]. Young cells, represented by dark dots, are found mainly on the two sides of

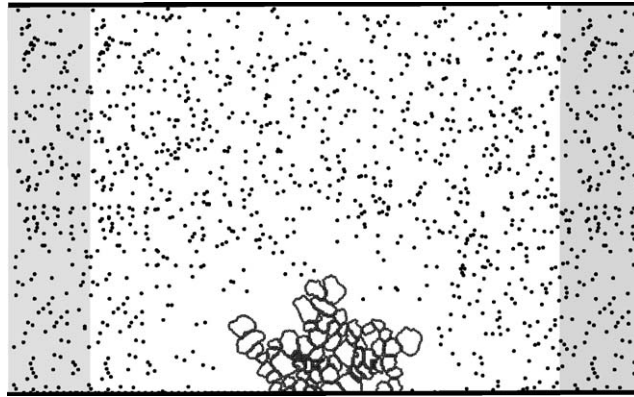


Fig. 15. Schematic representation of the simulation box. Horizontal walls restrict the motion in the y -direction, and periodic boundary conditions are used in the x -direction. The concentration of nutrient particles (dots) is kept constant in the zone of thickness d (shaded region). The values used in the simulations are: $L = 5000$ and $d = 100$. The colony starts by one cell touching the wall at the center of the zone of width L . We note a depletion region around the colony.

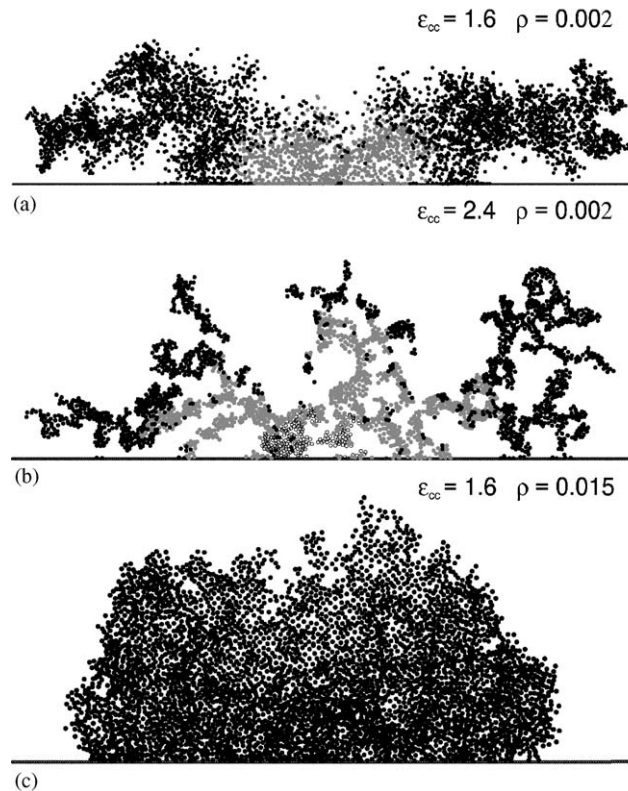


Fig. 16. Examples of colony morphologies obtained under different conditions: (a) a weak cell–cell interaction energy ($\epsilon_{cc} = 1.6$); (b) a strong cell–cell interaction energy ($\epsilon_{cc} = 2.4$); (c) high nutrient concentration ($\rho = 0.015$). Each circle represents one cell. The color of the cells is a function of their age (black being young, white being old and light gray being intermediate). The colonies contain a minimum of 3000 cells.

the colony. From this observation, we can conclude that the growth is not isotropic and is largely directed towards the nutrient reservoirs.

On the other hand, when the interaction is strong ($\epsilon_{cc} = 2.4$), the colony pattern exhibits ramified structures (Fig. 16b). In this case the growth is dominated by the value of ϵ_{cc} , and not only are there few cells adhering to

the wall but the branches are locally dense. The external branches are composed of young cells. This morphology is very similar to the structures obtained by 2D diffusion-limited aggregation (DLA) clusters [37].

A highly nutrient rich medium ($\rho = 0.015$) generates a compact and quasi-isotropic structure with a smooth contour (Fig. 16c). Furthermore, the adsorption surface of the colony on the wall is large compared to the previous structures. Here all the cells of the colony are young, i.e., the age distribution of the cells is very narrow, which indicates that the colony is growing rapidly.

The morphologies presented here have been described for *Bacillus subtilis* grown on a agar plate [38,39]. The authors have investigated the colony growth by varying the nutrient concentration and the substrate softness and have found five types of quasi-2D structures, including some that are quite similar to the three presented here.

4.2. Colony growth dynamics

Several parameters can affect the dynamics of biofilm growth. Of all these parameters, the nutrient concentration ρ is obviously the most straightforward. Fig. 17 shows a log–log plot of the number of cells $M(\tau)$ as a function of time for different values of ρ . The growth attains relatively rapidly a power law-regime. This growth is neither linear nor exponential, unlike the two behaviors previously reported [40]. The exponent obtained here increases with the nutrient concentration. The exponent actually increases towards the asymptotic value of 2, the result expected for a compact colony growing from its perimeter in a system without food depletion near the colony itself.

Another parameter which is important for the growth dynamics is the cell maturity age (t_{mature}). On Fig. 18 we report the results for three different values of t_{mature} . The data show that the growth exponent also increases with t_{mature} . Furthermore, we observe a step-profile for large values of t_{mature} , i.e., the colony grows in stages. This is a clear indication of the synchronization of the cell division process. Note that the largest colony size at a given time is obtained for $t_{\text{mature}} = 10^4$ over the simulation times used here, which means that the cell divides just after completing growth. Thus, this value is obviously close to the “natural” maturation age of the cells for these conditions.

5. Discussion

We have developed a 2D biofilm model using a novel single-cell based approach that represents cells as thermodynamic and mechanical autonomous systems. The current version of the model includes cell-division, cell-death, explicit presence of nutrients, as well as cell–wall and cell–cell interactions.

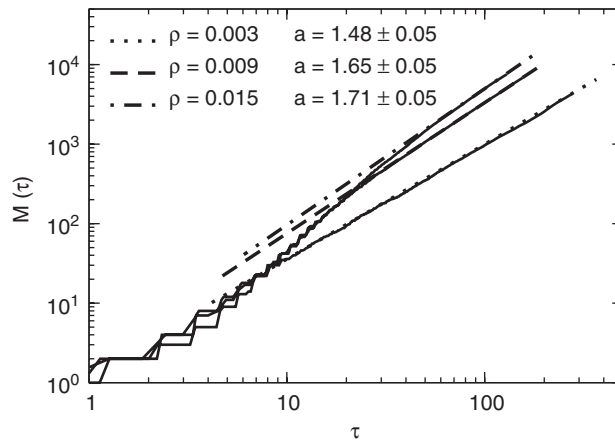


Fig. 17. Log–log plot of the number of cells versus time for three values of the concentration ρ . The growth quickly attains a power-law regime: $M(\tau) \sim \tau^a$.

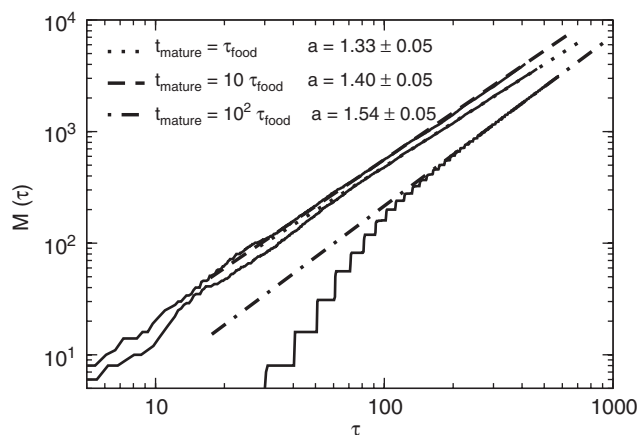


Fig. 18. Number of cells in the biofilm versus time for three values of the maturity age t_{mature} .

We first examined the physical characteristics of the cells in order to find the range of parameters needed to model realistic cells. Our investigation of the cell structural properties lead to results which could be compared to those obtained by other authors working on related polymer and/or colloidal systems. In addition, cell–wall and cell–cell interaction parameters have been studied, and two kinds of transitions have been pointed out: the unbinding–binding transition and the glassy transition. Our systematic study of the parameters of the model has helped us narrow the parameter phase space.

Different colony patterns can be created by changing some parameters such as the cell–cell interaction parameter and the nutrient concentration. These patterns are qualitatively similar to the ones found in the growth of *B. subtilis*. We have also found that growth dynamics is very sensitive to the nutrient concentration as well as to the cell maturity age (t_{mature}) and presents a power-law profile. These are preliminary results, and a more complete study of the model is in preparation.

Our model is now being modified to include a number of additional effects. First and foremost, the model will include several types of particles diffusing in the environment, such as neutral waste, toxic chemicals (which may include antibiotics), and signaling chemicals (necessary for quorum sensing). The cells will consume their resources for maintenance of their functions as well as for division (this is not currently the case), such that they can stop dividing or growing during long periods of starvation. The EPS will be allowed to be produced and detach from the cell, so that the free EPS chains will self-assemble into an EPS matrix. A more realistic model of a cell will include localized binding sites on its membrane (instead, all membrane monomers are currently sticky). We are also adding gravity (which will collapse some weak branched patterns) and cell motility. In order to better model the complex interactions between the different elements of this coarse-grained system, we are testing Monte Carlo methods that do not move all elements at the same frequency. Finally, and this is crucial, we are currently testing an evolutionary model of cells where the daughter cells differ slightly from the mother cell; cell division then favors certain traits and colonies become complex inhomogeneous living systems. Our approach is quite flexible and, in spite of the fact that it allows for detailed elements to be added, it remains computationally efficient. We believe that this provides an interesting alternative to the models currently used in this field.

Acknowledgements

We would like to acknowledge fruitful discussions with T. Beveridge, H. Eberl and J. Dutcher (University of Guelph). We would also like to thank HPCVL and Sharcnet for computing resources. This work was partially supported by Materials and Manufacturing Ontario (MMO) through their EMK program, and by the Advanced Food and Materials Network AFMnet.

References

- [1] B.E. Rittmann, P.L. McCarty, Model of steady-state-biofilm kinetics, *Biotechnol. Bioeng.* 22 (1980) 2343–2357.
- [2] O. Wanner, W. Gujer, Multispecies biofilm model, *Biotechnol. Bioeng.* 28 (1986) 314–328.
- [3] B.E. Rittmann, J.A. Manem, Development and experimental evaluation of a steady-state, multispecies biofilm model, *Biotechnol. Bioeng.* 39 (1992) 914–922.
- [4] O. Wanner, P. Reichert, Mathematical modeling of mixed-culture biofilms, *Biotechnol. Bioeng.* 49 (1996) 172–184.
- [5] J. Dockery, I. Klapper, Finger formation in biofilm layers, *SIAM J. Appl. Math.* 62 (2002) 853–869.
- [6] H.J. Eberl, C. Picioreanu, J.J. Heijnen, M.C.M. van Loosdrecht, A three-dimensional numerical study on the correlation of spatial structure, hydrodynamics conditions, and mass transfer and conversion in biofilms, *Chem. Eng. Sci.* 55 (2000) 6209–6222.
- [7] H.J. Eberl, D.F. Parker, M.C.M. van Loosdrecht, A new deterministic spatio-temporal continuum model for biofilm development, *J. Theor. Med.* 3 (2001) 161–175.
- [8] G.C. Barker, M.J. Grimson, A cellular automaton model of microbial growth, *Binary* 5 (1993) 132–137.
- [9] R.L. Colasanti, Cellular automata model of microbial colonies, *Binary* 4 (1992) 191–193.
- [10] G.B. Ermentrout, L. Edelstein-Keshet, Cellular automata approaches to biological modeling, *J. Theor. Biol.* 160 (1993) 97–133.
- [11] S.W. Hermanowicz, Model of two-dimensional biofilm morphology, *Water Sci. Technol.* 37 (1998) 219–222.
- [12] S.W. Hermanowicz, Two-dimensional simulations of biofilm development: effects of external environmental conditions, *Water Sci. Technol.* 39 (1999) 107–114.
- [13] D.R. Noguera, G. Pizarro, D.A. Stahl, B.E. Rittmann, Simulations of multispecies biofilm development in three dimensions, *Water Sci. Technol.* 39 (1999) 123–130.
- [14] C. Picioreanu, M.C.M. van Loosdrecht, J.J. Heijnen, A new combined differential-discrete cellular automaton for biofilm modeling: application for growth in gel beads, *Biotechnol. Bioeng.* 57 (1998) 718–731.
- [15] J.W.T. Wimpenny, R. Colasanti, A unifying hypothesis for the structure of microbial biofilms based on cellular automaton models, *FEMS Microbiol. Ecol.* 22 (1997) 1–16.
- [16] S.W. Hermanowicz, Biofilm structure: an interplay of models and experiments, in: S. Wuertz, P.A. Wilderer, P.L. Bishop (Eds.), *Biofilms in Wastewater Treatment: An Interdisciplinary Approach*, International Water Association Publishing, 2002, pp. 1–18.
- [17] J.U. Kreft, G. Booth, J.W.T. Wimpenny, Bacsim, a simulator for individual-based modelling of bacterial colony growth, *Microbiology* 144 (1998) 3275–3287.
- [18] J.-U. Kreft, C. Picioreanu, J.W.T. Wimpenny, M.C.M. van Loosdrecht, Individual-based modelling of biofilms, *Microbiology* 147 (2001) 2897–2912.
- [19] C. Picioreanu, J.-U. Kreft, M.C.M. van Loosdrecht, Particle-based multidimensional multispecies biofilm model, *Appl. Environ. Microbiol.* 70 (2004) 3024–3040.
- [20] I. Carmesin, K. Kremer, The bond fluctuation method: a new effective algorithm for the dynamics of polymers in all spatial dimensions, *Macromolecules* 21 (1988) 2819–2823.
- [21] N. Metropolis, A.W. Rosenbluth, M.N. Rosenbluth, A.H. Teller, E. Teller, Equation of state calculations by fast computing machines, *J. Chem. Phys.* 21 (1953) 1087–1092.
- [22] I. Teraoka, *Polymer Solutions*, Wiley-Interscience, New York, 2001.
- [23] S. Leibler, R.R.P. Singh, M.E. Fisher, Thermodynamic behaviour of two-dimensional vesicles, *Phys. Rev. Lett.* 59 (1987) 1989–1992.
- [24] A.C. Maggs, S. Leibler, M.E. Fisher, C.J. Camacho, Size of an inflated vesicle in two dimensions, *Phys. Rev. A* 42 (1990) 691–695.
- [25] C. Picioreanu, M.C.M. van Loosdrecht, J.J. Heijnen, Modelling and predicting biofilm structure, in: D.G. Allison, P. Gilbert, H.M. Lappin-Scott, M. Wilson (Eds.), *Community Structure and Co-operation in Biofilms*, Cambridge University Press, Cambridge, UK, 2000, pp. 129–166.
- [26] S.W. Hermanowicz, A simple 2d biofilm model yields a variety of morphological features, *Math. Biosci.* 169 (2001) 1–14.
- [27] D.G. Davies, M.R. Parsek, B.H. Iglewski, J.W. Costerton, E.P. Greenberg, The involvement of cell-to-cell signals in the development of a bacterial biofilm, *Science* 280 (1998) 295–298.
- [28] R. Kolter, R. Losik, One for all and all for one, *Science* 280 (1998) 226–227.
- [29] C.J. Camacho, M.E. Fisher, Tunable fractal shapes in self-avoiding polygons and planar vesicles, *Phys. Rev. Lett.* 65 (1990) 9–12.
- [30] P.G. de Gennes, *Scaling Concept in Polymer Physics*, Cornell University Press, Ithaca, NY, 1979.
- [31] Y. Kantor, Properties of tethered surfaces, in: D. Nelson, T. Piran, S. Weinberg (Eds.), *Statistical Mechanics of Membranes and Surfaces*, World Scientific, Singapore, 1989, pp. 115–136.
- [32] U. Seifert, R. Lipowsky, Adhesion of vesicles, *Phys. Rev. A* 42 (1990) 4768–4771.
- [33] H.-G. Döbereiner, B. Dubin-Thaler, G. Giannone, H.S. Xenias, M.P. Sheetz, Dynamic phase transitions in cell spreading, *Phys. Rev. Lett.* 93 (2004) 108105-1.
- [34] W. Helfrich, Out-of-plane fluctuations of lipid bilayers, *Z. Naturforsch.* 30c (1975) 841–842.
- [35] W. Helfrich, R.-M. Servuss, Undulations steric interaction and cohesion of fluid membranes, *Nuovo Cimento* 3D (1984) 137–151.
- [36] F. Family, T. Vicsek, *Dynamic of Fractal Surfaces*, World Scientific, Singapore, 1991.
- [37] T.A. Witten, L.M. Sander, Diffusion-limited aggregation, a kinetic critical phenomenon, *Phys. Rev. Lett.* 47 (1981) 1400.
- [38] M. Matsushita, H. Fugikawa, Diffusion-limited growth in bacterial colony formation, *Physica A* 168 (1990) 498–506.
- [39] M. Matsushita, J. Wakita, H. Itoh, K. Watanabe, T. Arai, T. Matsuyama, H. Sakaguchi, M. Mimura, Formation of colony patterns by a bacterial cell population, *Physica A* 274 (1999) 190–199.
- [40] J.C.M. Mombach, N. Lemke, B.E.J. Bodmann, M.A.P. Idiart, A mean-field theory of cellular growth, *Europhys. Lett.* 59 (2002) 923–928.